



HAL
open science

General approaches for shear-correcting coordinate transformations in Bragg coherent diffraction imaging: Part 2

P. Li, S. Maddali, A. Pateras, I. Calvo-Almazan, S.O. Hruszkewycz, V. Chamard, M. Allain

► To cite this version:

P. Li, S. Maddali, A. Pateras, I. Calvo-Almazan, S.O. Hruszkewycz, et al.. General approaches for shear-correcting coordinate transformations in Bragg coherent diffraction imaging: Part 2. *Journal of Applied Crystallography*, 2020, 53, pp.404. hal-02338385

HAL Id: hal-02338385

<https://hal.science/hal-02338385v1>

Submitted on 9 Mar 2020

HAL is a multi-disciplinary open access archive for the deposit and dissemination of scientific research documents, whether they are published or not. The documents may come from teaching and research institutions in France or abroad, or from public or private research centers.

L'archive ouverte pluridisciplinaire **HAL**, est destinée au dépôt et à la diffusion de documents scientifiques de niveau recherche, publiés ou non, émanant des établissements d'enseignement et de recherche français ou étrangers, des laboratoires publics ou privés.

General approaches for shear-correcting coordinate transformations in Bragg coherent diffraction imaging. Part II

P. Li,^a S. Maddali,^b A. Pateras,^{c,d} I. Calvo-Almazan,^b S.O. Hruszkewycz,^b W. Cha,^e V. Chamard^a and M. Allain^{a*}

Received 15 August 2019
Accepted 31 January 2020

Edited by S. Sasaki, Tokyo Institute of Technology, Yokohama, Japan

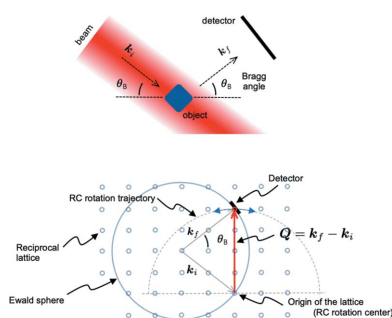
Keywords: Bragg coherent diffraction imaging; Fourier synthesis; non-orthogonal Fourier sampling; coordinate transformation; shear correction; Bragg ptychography.

^aAix-Marseille Univ., CNRS, Centrale Marseille, Institute Fresnel, 13013 Marseille, France, ^bMaterials Science Division, Argonne National Laboratory, Lemont, IL 60439, USA, ^cCenter for Integrated Nanotechnologies, Los Alamos National Laboratory, Los Alamos, NM 87545, USA, ^dMaterials Science and Technology Division, Los Alamos National Laboratory, Los Alamos, NM 87545, USA, and ^eX-ray Science Division, Argonne National Laboratory, Lemont, IL 60439, USA.
*Correspondence e-mail: marc.allain@fresnel.fr

X-ray Bragg coherent diffraction imaging (BCDI) has been demonstrated as a powerful 3D microscopy approach for the investigation of sub-micrometre-scale crystalline particles. The approach is based on the measurement of a series of coherent Bragg diffraction intensity patterns that are numerically inverted to retrieve an image of the spatial distribution of the relative phase and amplitude of the Bragg structure factor of the diffracting sample. This 3D information, which is collected through an angular rotation of the sample, is necessarily obtained in a non-orthogonal frame in Fourier space that must be eventually reconciled. To deal with this, the approach currently favored by practitioners (detailed in Part I) is to perform the entire inversion in conjugate non-orthogonal real- and Fourier-space frames, and to transform the 3D sample image into an orthogonal frame as a post-processing step for result analysis. In this article, which is a direct follow-up of Part I, two different transformation strategies are demonstrated, which enable the entire inversion procedure of the measured data set to be performed in an orthogonal frame. The new approaches described here build mathematical and numerical frameworks that apply to the cases of evenly and non-evenly sampled data along the direction of sample rotation (*i.e.* the rocking curve). The value of these methods is that they rely on the experimental geometry, and they incorporate significantly more information about that geometry into the design of the phase-retrieval Fourier transformation than the strategy presented in Part I. Two important outcomes are (1) that the resulting sample image is correctly interpreted in a shear-free frame and (2) physically realistic constraints of BCDI phase retrieval that are difficult to implement with current methods are easily incorporated. Computing scripts are also given to aid readers in the implementation of the proposed formalisms.

1. Introduction

Coherent diffraction imaging (CDI) approaches based on X-ray Bragg diffraction have emerged as valuable tools for materials science, owing to their sensitivity to atomic displacement fields, their 3D imaging capability, their high spatial resolution (Robinson *et al.*, 2003) and their suitability for nondestructive investigation of complex material systems in various environments (Ulvestad *et al.*, 2015). These methods, including single-particle Bragg coherent diffraction imaging (BCDI) (Williams *et al.*, 2003; Pfeifer *et al.*, 2006) and Bragg ptychography (Godard *et al.*, 2011; Hruszkewycz *et al.*, 2012; Mastropietro *et al.*, 2017), rely on the measurement of far-field X-ray coherent intensity patterns in the vicinity of a Bragg peak that result from a crystalline sample being illuminated with a coherent X-ray beam. One unique aspect of BCDI as



compared to forward-scattering 3D CDI approaches (Chapman & Nugent, 2010; Miao *et al.*, 2015) is the way the information is obtained. In a Bragg diffraction geometry, the 3D information is gathered through a series of 2D measurements, which correspond to closely spaced sequential parallel planar slices of the Fourier-space 3D intensity pattern. Thus, the stacking of the 2D measurements produces a 3D intensity dataset that contains information about the 3D structural features of the diffracting sample. This dataset is numerically inverted to yield a 3D real-space array that describes the sample structure.

However, one important consideration in BCDI is the fact that the directions of Fourier-space sampling of a BCDI scan are necessarily non-orthogonal (as discussed in Part I). This holds true for the cases when the data are obtained using an angular sample scan (along the rocking curve or RC) (Williams *et al.*, 2003) or an incident-beam energy scan (Cha *et al.*, 2016). The inherent non-orthogonal nature of the Fourier-space measurement has to be accounted for when interpreting the retrieved image of the 3D sample. One strategy to deal with the non-orthogonal measurement frame is presented in Part I of this work and is summarized here. The coherent far-field diffraction from a scatterer in the Bragg condition is the squared modulus of the Fourier transform of the complex-valued 3D scatterer (Takagi, 1969; Vartanyants & Robinson, 2001), centered at the Bragg peak of interest. The fact that measurement of such a Bragg peak is necessarily performed on a non-orthogonal basis in Fourier space implies that the resultant real-space sample is likewise described in a conjugate sheared frame. Thus, a real-space transformation, which we formally derive in Part I, must be applied after the completion of phase retrieval in order to visualize the sample in an orthogonal frame (Berenguer *et al.*, 2013; Yang *et al.*, 2019). This approach is the one typically implemented in most of the Bragg CDI literature published to date (Pfeifer *et al.*, 2006; Ulvestad *et al.*, 2015).

The motivation for Part II is born of a realization that the approach of rectifying the frame of the sample after phase retrieval, though commonly implemented in BCDI, significantly limits the ability to incorporate constraints stemming from the physics of the experiment or from the geometry of the sample into the phase-retrieval process. For example, the behavior of the commonly utilized shrinkwrap algorithm (Marchesini *et al.*, 2003) could be much more carefully controlled if the blurring kernel were not cast in dimension- and direction-agnostic ‘pixel’ coordinates, as it is today, but rather in real-space units that impact all facets and corners of the reconstructed object symmetrically in three dimensions. Similarly, efforts to date to account for partial coherence effects in BCDI data have treated the problem as an *ad hoc* blind ‘deblurring’ problem (Clark *et al.*, 2012) rather than building in estimates based on known de-cohering effects that can be calculated for X-ray synchrotron beamlines. Additionally, when considering Bragg CDI methods more broadly, working in a sheared sample frame greatly complicates the description and placement of a localized beam in rocking-curve 3D Bragg ptychography methods (Hill *et al.*, 2018;

Hruszkewycz *et al.*, 2012). Solutions to these and other related problems all hinge on a phase-retrieval description of the sample on an orthogonal real-space reference frame onto which other experimental constraints and models map naturally. A recent example wherein such a strategy was utilized to determine the angular uncertainty of each measurement step in a rocking curve during the course of image reconstruction with phase retrieval (Calvo-Almazán *et al.*, 2019) shows the potential of such a construction. We anticipate that further advances of this nature could be possible, provided that formalisms for experimental-geometry-aware Fourier transformations are developed and provided to the community.

In this article we present the framework for two computationally efficient Fourier transformations that simultaneously offer a natural frame both for the sample (orthogonal real-space frame) and for the data (non-orthogonal rocking-curve sampling of Fourier space) and that can be integrated into common phase-retrieval algorithms. The first method is derived for the case where an evenly sampled data set is obtained by typical rocking-curve measurement methods. It is based on a physically informed description of the conjugate relations between the 3D real and Fourier spaces that is compatible with computationally efficient discrete Fourier transformations. The second approach, which has been introduced and used in earlier Bragg CDI-related work (Hruszkewycz *et al.*, 2017; Hill *et al.*, 2018; Calvo-Almazán *et al.*, 2019), is more flexible and is built on a concept that exploits the properties of Fourier-slice projection. For the sake of clarity, in building our calculations, we adopt the relatively simple though highly utilized case of symmetric X-ray diffraction with a two-circle diffractometer (sometimes referred to as symmetric θ - 2θ geometry). The extension to the nonsymmetric case involving more than two diffractometer angles, as was dealt with in Part I, is relatively straightforward and is described in Appendix A.

2. The coordinate transform and conjugation relation

We briefly summarize the conjugate relation between coordinate representations of real and Fourier spaces. We refer the reader to Part I for further details.¹

We denote by $\tilde{\mathbf{r}} := [\tilde{r}_1 \ \tilde{r}_2 \ \tilde{r}_3]^T$ a point in real or direct space that is defined with respect to a frame $(\tilde{\mathbf{e}}_1, \tilde{\mathbf{e}}_2, \tilde{\mathbf{e}}_3)$. Here ‘T’ denotes the matrix transpose. Similarly, we denote by $\tilde{\mathbf{q}} := [\tilde{q}_1 \ \tilde{q}_2 \ \tilde{q}_3]^T$ a point in Fourier space (*i.e.* associated with the measurement) defined with respect to a frame $(\tilde{\mathbf{k}}_1, \tilde{\mathbf{k}}_2, \tilde{\mathbf{k}}_3)$. In addition, we define the Fourier pair $\tilde{\psi} \rightleftharpoons \tilde{\Psi}$ by

$$\tilde{\Psi}(\tilde{\mathbf{q}}) = \int_{\mathbb{R}^3} \tilde{\psi}(\tilde{\mathbf{r}}) \exp(-i2\pi\tilde{\mathbf{r}}^T\tilde{\mathbf{q}}) \, d\tilde{\mathbf{r}}, \quad (1)$$

¹ We adopt the notations and conventions used in Part I, with a single adaptation: all frames introduced in Part II are built with unit-norm vectors by default, and therefore we drop the caret symbol ‘ˆ’ in the unit-norm vector notation, *e.g.* the unit-norm vectors $\hat{\mathbf{e}}$, $\hat{\mathbf{k}}$ and $\hat{\mathbf{k}}$ introduced in this section are unambiguously written hereafter as \mathbf{e} , \mathbf{e} , \mathbf{k} and \mathbf{k} , unless explicitly stated otherwise.

where $\iota = (-1)^{1/2}$. This relationship implies that $(\tilde{\mathbf{e}}_1, \tilde{\mathbf{e}}_2, \tilde{\mathbf{e}}_3)$ and $(\tilde{\mathbf{k}}_1, \tilde{\mathbf{k}}_2, \tilde{\mathbf{k}}_3)$ are dual, or conjugate, frames. The field $\tilde{\Psi}$ can be represented in any other (Fourier-space) frame $(\mathbf{k}_1, \mathbf{k}_2, \mathbf{k}_3)$ through an appropriate linear coordinate transformation. We can obtain such an alternative frame of representation on a new Fourier-space basis by applying a linear transformation:

$$\mathbf{q} = \mathbf{B}_q \tilde{\mathbf{q}}. \quad (2)$$

In this expression, $\mathbf{B}_q \in \mathbb{R}^{3 \times 3}$ is the ‘original’ Fourier frame $(\tilde{\mathbf{k}}_1, \tilde{\mathbf{k}}_2, \tilde{\mathbf{k}}_3)$ expressed in the ‘new’ Fourier frame $(\mathbf{k}_1, \mathbf{k}_2, \mathbf{k}_3)$. With a change of frame in \mathbf{q} also comes a change in the dual (real-space) basis frame $(\mathbf{e}_1, \mathbf{e}_2, \mathbf{e}_3)$ in which the vector $\mathbf{r} := [r_1 \ r_2 \ r_3]^T$ is expressed. As in Fourier space, the reframed real-space variable \mathbf{r} is related to $\tilde{\mathbf{r}}$ by a linear coordinate transform:

$$\mathbf{r} = \mathbf{B}_r \tilde{\mathbf{r}}, \quad (3)$$

with $\mathbf{B}_r \in \mathbb{R}^{3 \times 3}$. For the sake of simplicity, from now on we adopt the simplified notation $\mathbf{B}_r \equiv \mathbf{B}$ in this paper. From Part I (see Section 2), the real-space linear transformation and its Fourier-space counterpart are related by

$$\mathbf{B}_q = \mathbf{B}^{-T} \quad (4)$$

with $\mathbf{B}^{-T} = (\mathbf{B}^T)^{-1} = (\mathbf{B}^{-1})^T$, and the coordinate transformations in Fourier space can be implemented by the following relationships:

$$\Psi(\mathbf{q}) = \det(\mathbf{B}) \tilde{\Psi}(\mathbf{B}^T \mathbf{q}) \Leftrightarrow \tilde{\Psi}(\tilde{\mathbf{q}}) = \frac{1}{\det(\mathbf{B})} \Psi(\mathbf{B}^{-T} \tilde{\mathbf{q}}). \quad (5)$$

As shown in Part I, because of the Fourier relationship $\psi \Leftarrow \Psi$, the means of coordinate transformation in real space are determined to be $\psi(\mathbf{r}) := \tilde{\psi}(\mathbf{B}^{-1} \mathbf{r})$. The functions $\tilde{\psi}$ and ψ actually represent the same real-space object but in different frames. The same holds true for $\tilde{\Psi}$ and Ψ regarding the Fourier-space representation. The equations in (5) are therefore pivotal as they describe how any measurement in $(\tilde{\mathbf{k}}_1, \tilde{\mathbf{k}}_2, \tilde{\mathbf{k}}_3)$ can be mapped to an alternative frame $(\mathbf{k}_1, \mathbf{k}_2, \mathbf{k}_3)$, and *vice versa*. In particular, in the subsequent sections, we show the means by which to construct BCDI-compatible transformations that work within an alternative orthogonal frame that is built upon the specific geometric considerations of the experiment.

3. Application to BCDI: from a non-orthogonal to an orthogonal frame

In this section, we begin by considering the specific geometry involved in a simple BCDI measurement implemented in a symmetric two-circle reflection geometry (see Fig. 1). We assume that the measurement is performed in the far-field regime and that the kinematic approximation applies. Therefore, the exit field $\tilde{\psi}$ and the diffracted field $\tilde{\Psi}$ are related by a 3D Fourier transformation. An important feature of the Bragg geometry is that making small changes in the angular orientation of the sample with respect to the incident-beam direction allows the intensity of the diffracted field $\tilde{\Psi}$ to be measured in three dimensions. However, the direction of Fourier-space scanning along the rocking curve is not perpendicular to the detection plane (as demonstrated in Part I). Thus, the measurement of $|\tilde{\Psi}|^2$ corresponds to a non-orthogonal Fourier-space frame $(\tilde{\mathbf{k}}_1, \tilde{\mathbf{k}}_2, \tilde{\mathbf{k}}_3)$. The frame corresponding to the specific BCDI geometry we are considering is shown in Fig. 2(a). The dual conjugate real-space frame $(\tilde{\mathbf{e}}_1, \tilde{\mathbf{e}}_2, \tilde{\mathbf{e}}_3)$ is also non-orthogonal (Berenguer *et al.*, 2013; Yang *et al.*, 2019) and is also shown for our case in Fig. 1(a). As a result, the 3D inverse Fourier transform (IFT) of $\tilde{\Psi}$ provides a rather unintuitive representation of the exit field $\tilde{\psi}$.

To obtain an image of the sample on a natural orthogonal frame, one possible solution is to generate a pseudo-dataset derived by interpolating the measured pixelated intensity data onto a chosen orthogonal-frame Fourier space $(\mathbf{k}_1, \mathbf{k}_2, \mathbf{k}_3)$. Given this type of dataset as an input, standard BCDI reconstruction algorithms would produce a 3D image of the object expressed in orthogonal coordinates. In practice, however, systematic errors are likely to be encountered

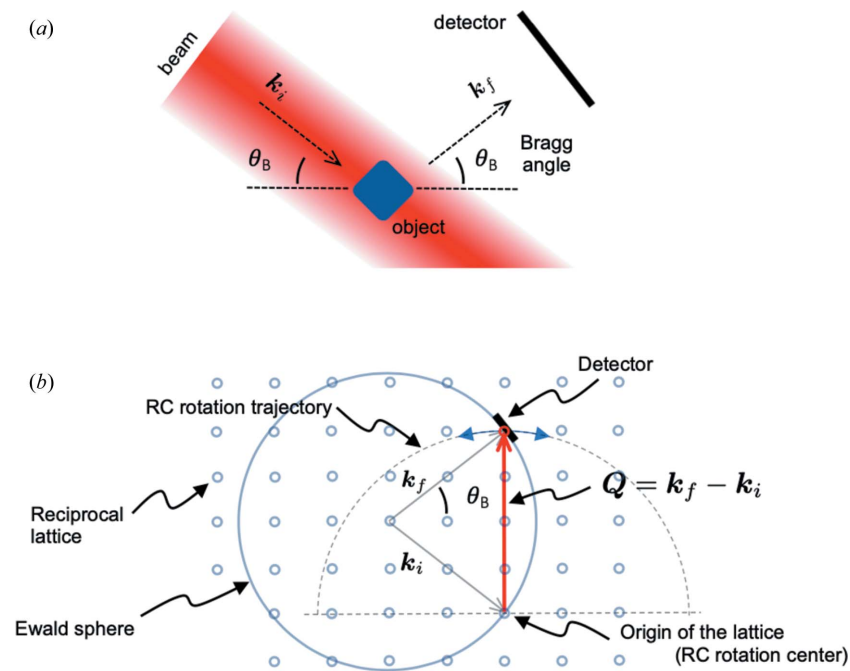


Figure 1 Bragg coherent diffraction: geometry. (a) A typical X-ray coherent diffraction imaging experiment can be described by a crystalline sample illuminated by a plane wave with incident vector \mathbf{k}_i and by a detector normal to the exit vector \mathbf{k}_f . (b) In addition, the vector pair $(\mathbf{k}_i, \mathbf{k}_f)$ are in the ‘Bragg condition’: the momentum transfer vector $\mathbf{q} := \mathbf{k}_f - \mathbf{k}_i$ coincides with a point in the reciprocal lattice, hence defining a Bragg angle θ_B . During the rocking curve, the rotation of the reciprocal lattice about its origin brings the probed Bragg peak through the detector surface.

owing to the interpolation of low-count-rate regions of the data that are present in most BCDI measurements. An alternative approach can be imagined by considering the equations in (5). They suggest that the evaluated far field $\tilde{\Psi}$ that is commensurate with the measurement on average, and not the data itself, can be interpolated onto $(\mathbf{k}_1, \mathbf{k}_2, \mathbf{k}_3)$, hence providing an orthogonal real-space representation. Below, we aim to develop a computationally efficient transformation strategy based on this concept. We take advantage of the fact that the measurement frame shown in Fig. 2(a) is actually very closely related to the orthonormal frame shown in Fig. 2(b). The desired orthonormal frame $(\mathbf{k}_1, \mathbf{k}_2, \mathbf{k}_3)$ differs from $(\tilde{\mathbf{k}}_1, \tilde{\mathbf{k}}_2, \tilde{\mathbf{k}}_3)$ by a unique rotation of $\tilde{\mathbf{k}}_3$ about the axis defined by $\tilde{\mathbf{k}}_1$. Because of this relatively simple rotational relationship, the interpolation between the two frames can be performed very efficiently, making it suitable to embed within an iterative phase-retrieval algorithm.

In the next section, we show how this interpolation can be implemented with continuous Fourier transform operators; we start with a continuous framework because it is the natural way to account for normalization factors and meshing constraints that would be lost otherwise. Following that, a practical numerical implementation is derived.

3.1. Continuous derivation with Fourier operators

Our aim is to use the orthogonal frame $(\mathbf{e}_1, \mathbf{e}_2, \mathbf{e}_3)$ depicted in Fig. 2(b) as our resultant real-space representation frame. Starting in this frame makes the Fourier pair $\psi \rightleftharpoons \Psi$ readily available by application of a Fourier transformation. However, one cannot incorporate such a transformation into an iterative phase-retrieval image reconstruction algorithm because the far field Ψ is described in a frame not consistent with the rocking-curve measurement [as shown in Figs. 4(a) and 4(c) in Section 3.3]. To solve this problem, we aim to provide a direct mapping from the orthogonally represented ψ to the non-orthogonal $\tilde{\Psi}$. We start by explicitly deriving equation (2), which describes the relationship between \mathbf{q} and $\tilde{\mathbf{q}}$ for the two-circle symmetric diffraction geometry that we consider by way of example. From Fig. 2, we have

$$\mathbf{B}_q = \begin{pmatrix} 1 & 0 & 0 \\ 0 & 1 & -\sin \theta_B \\ 0 & 0 & \cos \theta_B \end{pmatrix}. \quad (6)$$

Applying equation (5) then yields

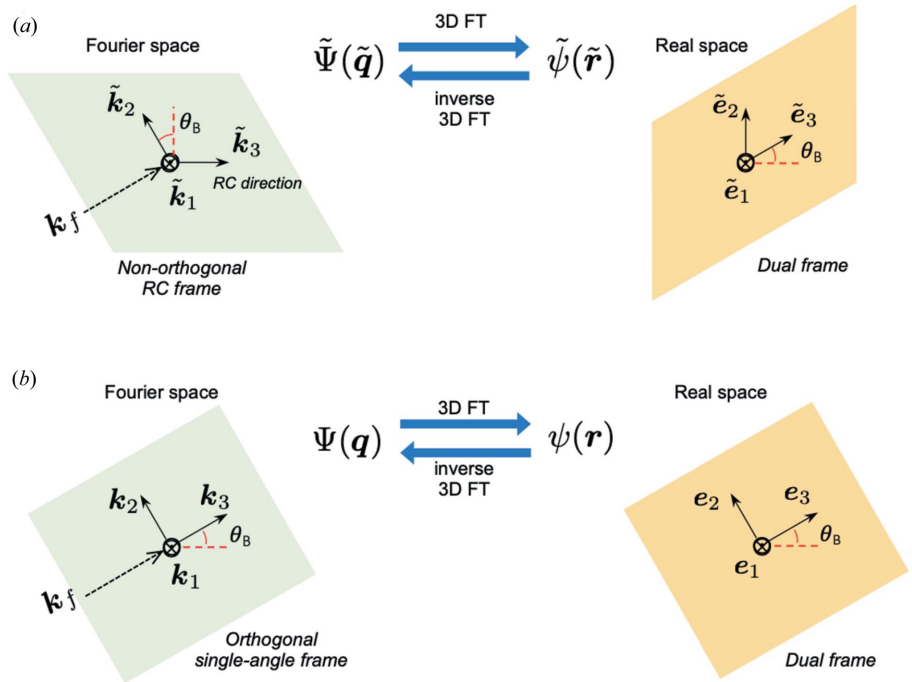


Figure 2

Bragg coherent diffraction: frame definitions. (a) As long as small angular ranges are considered, the rocking-curve measurement is equivalent to scanning the (intensity of the) Fourier-space function $\tilde{\Psi}$ along the direction $\tilde{\mathbf{k}}_3$ (left). As a result, $\tilde{\Psi}$ has a dual representation in real space $\tilde{\psi}$ that is non-orthogonal (right). (b) From $(\tilde{\mathbf{k}}_1, \tilde{\mathbf{k}}_2, \tilde{\mathbf{k}}_3)$, another orthogonal frame $(\mathbf{k}_1, \mathbf{k}_2, \mathbf{k}_3)$ can be obtained from the rotation of the vector $\tilde{\mathbf{k}}_3$ so that it aligns with the exit direction \mathbf{k}_f (left). The representation of the 3D far field in this system is denoted Ψ and corresponds to an orthogonal representation of the exit field ψ (right).

$$\tilde{\Psi}(\tilde{\mathbf{q}}) = \cos \theta_B \Psi(\tilde{q}_1, \tilde{q}_2 - \tilde{q}_3 \sin \theta_B, \tilde{q}_3 \cos \theta_B). \quad (7)$$

The relation above is precisely the mapping $\psi \rightarrow \tilde{\Psi}$ that is needed. It allows the ‘non-orthogonal’ far field $\tilde{\Psi}$ to be derived from the ‘orthogonal’ representations $\psi \rightleftharpoons \Psi$ [see Figs. 4(a) and 4(d) below]. In addition, we have

$$\begin{aligned} & \Psi(\tilde{q}_1, \tilde{q}_2 - \tilde{q}_3 \sin \theta_B, \tilde{q}_3 \cos \theta_B) \\ & := \int_{\mathbb{R}^3} \psi(\mathbf{r}) \exp\{-i2\pi[r_1\tilde{q}_1 + r_2(\tilde{q}_2 - \tilde{q}_3 \sin \theta_B) + r_3\tilde{q}_3 \cos \theta_B]\} d\mathbf{r} \\ & = \int_{\mathbb{R}^2} \xi(\mathbf{r}_\perp, \tilde{q}_3 \cos \theta_B) \exp(-i2\pi\mathbf{r}_\perp^\top \tilde{\mathbf{q}}_\perp) d\mathbf{r}_\perp \\ & = [\mathcal{F}_\perp \xi](\tilde{\mathbf{q}}_\perp, \tilde{q}_3 \cos \theta_B). \end{aligned} \quad (8)$$

In these expressions, the coordinates $\tilde{\mathbf{q}}_\perp := (\tilde{q}_1, \tilde{q}_2)$ are parallel to the pixel sampling directions in the measurement plane and are conjugated to $\mathbf{r}_\perp = (r_1, r_2)$. Our aim is to define an intermediate function ξ that preserves the behavior and 3D nature of ψ , and which can also be acted upon by a 2D Fourier transform (FT) \mathcal{F}_\perp that acts on the first and second spatial coordinates \mathbf{r}_\perp . This can be done by defining the following:

$$\xi(\mathbf{r}_\perp, q_3) := [\mathcal{F}_3 \psi](\mathbf{r}_\perp, q_3) \exp(i2\pi r_2 q_3 \tan \theta_B) \quad (9)$$

with \mathcal{F}_3 the 1D FT operator acting along the third spatial coordinate r_3 . Finally, (7) and (8) can be combined so that we obtain

$$\tilde{\Psi}(\tilde{\mathbf{q}}) = \cos \theta_B [\mathcal{F}_\perp \xi](\mathbf{q}_\perp = \tilde{\mathbf{q}}_\perp, q_3 = \tilde{q}_3 \cos \theta_B). \quad (10)$$

By examining (9) and (10), we see that three distinct steps are required to compute the non-orthogonal far field $\tilde{\Psi}$ starting from the real-space orthogonal representation ψ . They can be described as (i) a one-dimensional FT, which provides $\mathcal{F}_3 \psi$; (ii) a pointwise multiplication with a spatially varying phase term; and (iii) an FT acting on two of the three axes, which provides $\tilde{\Psi}$. Considering the problem in terms of these steps indicates a clear path towards numerical implementation. Furthermore, the computational burden involved in such a calculation of $\tilde{\Psi}$ from ψ is similar to a single 3D digital FT. This opens up the possibility of incorporating such a computation within an iterative reconstruction algorithm without adding a significant time penalty and enabling natural frames in both real and Fourier spaces to be enforced from the outset. This provides distinct benefits, outlined in Section 1, that cannot be realized with the approach presented in Part I.

In the context of typical iterative phase-retrieval algorithms, we need to define not only the ‘forward’ calculation of $\tilde{\Psi}$ from ψ [as in relation (10)] but also a ‘backward’ step that computes ψ from $\tilde{\Psi}$. This backward step can be deduced from (8) and (9) by adopting an intermediate variable ζ that mimics the form of ξ :

$$\psi = \frac{1}{\cos \theta_B} [\mathcal{F}_3^{-1} \zeta] \quad (11)$$

with

$$\begin{aligned} \zeta(\mathbf{r}_\perp, q_3) &:= [\mathcal{F}_\perp^{-1} \tilde{\Psi}](\tilde{\mathbf{r}}_\perp = \mathbf{r}_\perp, \tilde{q}_3 = q_3 / \cos \theta_B) \\ &\times \exp(-i2\pi r_2 q_3 \tan \theta_B). \end{aligned} \quad (12)$$

We note from (7) the ability to ‘shear’ and ‘unshear’ the Fourier frame *via* a continuous shifting of the $(\mathbf{k}_1, \mathbf{k}_2)$ plane as the position along \mathbf{k}_3 changes. This continuous Fourier shifting is actually performed not in Fourier space but in real space *via* the modulation with the complex exponential terms in the expressions of ξ and ζ , given by (9) and (12), respectively. The above derivation leads to several important insights:

(1) If a more complex transformation were considered, for example a rotation of two vectors in the basis rather than one, the ability to perform this interpolation *via* a phase ramp would be lost and the computational complexity of the alternative approach would increase significantly.

(2) The frame shown in Fig. 2(b) is not the only orthogonal frame that one can build from a single rotation. Interestingly, another orthogonal frame is obtained by the clockwise rotation by θ_B of the vector \mathbf{k}_2 about \mathbf{k}_1 , which, consequently, gives an alternative orthogonal real-space frame. This frame may be convenient if symmetric Bragg reflections are involved, because it often matches a natural ‘laboratory frame’. The derivation of the alternative mapping is a straightforward adaptation of the equations given above, and it is not derived here.

(3) Let us recall that we restricted our presentation to symmetric Bragg reflections only for the sake of simplicity. Actually, our strategy can deal with any Bragg peak: in a general Bragg scattering geometry, obtained with diffract-

ometers with more degrees of freedom, the vector $\tilde{\mathbf{k}}_3$ defining the Fourier-space scanning direction of the RC will have a nonzero projection along \mathbf{k}_1 , which is very easy to address with a straightforward adaptation of our approach. The extension of the equations presented in this section to such a situation is presented in Appendix A.

We end by pointing out that the derivations presented above were obtained with operators defined over continuous domains. For the practical application to experimental data, we now consider their numerical evaluation *via* the discrete Fourier transform (DFT).

3.2. Implementation with discrete Fourier transforms

Let us recall first the results obtained in the previous section: the forward mapping (from ψ to $\tilde{\Psi}$) is given by

$$\begin{cases} \xi(\mathbf{r}_\perp, q_3) = [\mathcal{F}_3 \psi](\mathbf{r}_\perp, q_3) \exp(i2\pi r_2 q_3 \tan \theta_B) \\ \tilde{\Psi}(\tilde{\mathbf{q}}) = \cos \theta_B [\mathcal{F}_\perp \xi](\tilde{\mathbf{q}}_\perp, \tilde{q}_3 \cos \theta_B) \end{cases} \quad (13)$$

and the backward mapping (from $\tilde{\Psi}$ to ψ) by

$$\begin{cases} \zeta(\mathbf{r}_\perp, q_3) = [\mathcal{F}_\perp^{-1} \tilde{\Psi}](\mathbf{r}_\perp, q_3 / \cos \theta_B) \exp(-i2\pi r_2 q_3 \tan \theta_B) \\ \psi(\mathbf{r}) = (1 / \cos \theta_B) [\mathcal{F}_3^{-1} \zeta](\mathbf{r}) \end{cases} \quad (14)$$

where ξ and ζ are intermediate functions designed to enable convenient separation of the 3D Fourier transformation integral into sequential operations involving 2D and 1D Fourier transformations. The relations (13) and (14) will be evaluated numerically over orthogonal frames, hence requiring that both the direct-space and Fourier-space domains are defined over consistent rectangular meshes. In real space, this regular mesh can be expressed by

$$\mathbf{r} \in \{\Lambda_r \mathbf{n}\} \quad \text{where} \quad \Lambda_r = \begin{bmatrix} \delta_{r_1} & & \\ & \delta_{r_2} & \\ & & \delta_{r_3} \end{bmatrix}, \quad (15)$$

with $\mathbf{n} := [n_1 \ n_2 \ n_3]^T \in \mathbb{Z}^3$ the real-space sample index and δ_{r_1} , δ_{r_2} and δ_{r_3} the real-space sampling rates along \mathbf{e}_1 , \mathbf{e}_2 and \mathbf{e}_3 , respectively. Similarly, the Fourier-space mesh is defined by

$$\mathbf{q} \in \{\Lambda_q \mathbf{m}\} \quad \text{where} \quad \Lambda_q = \begin{bmatrix} \delta_{q_1} & & \\ & \delta_{q_2} & \\ & & \delta_{q_3} \end{bmatrix}. \quad (16)$$

Here, $\mathbf{m} := [m_1 \ m_2 \ m_3]^T \in \mathbb{Z}^3$ is the Fourier-space pixel index and δ_{q_1} , δ_{q_2} and δ_{q_3} are the Fourier-space sampling rates along \mathbf{k}_1 , \mathbf{k}_2 and \mathbf{k}_3 , respectively. We should also account for the fact that (13) and (14) will be computed by DFTs. In that case, our construction must adhere to the following constraint, which stipulates that the sampling rates in real and Fourier space are related:

$$\mathbf{r}^T \mathbf{q} = \mathbf{n}^T \Lambda_r \Lambda_q \mathbf{m} = \mathbf{n}^T \mathcal{D} \mathbf{m} \quad \text{with} \quad \mathcal{D} = \begin{bmatrix} N_1^{-1} & & \\ & N_2^{-1} & \\ & & N_3^{-1} \end{bmatrix}. \quad (17)$$

In this equation, N_1 , N_2 and N_3 are the number of sample points in real space and in Fourier space, corresponding to the directions \mathbf{e}_1 and \mathbf{k}_1 , \mathbf{e}_2 and \mathbf{k}_2 , and \mathbf{e}_3 and \mathbf{k}_3 , respectively. With the above construction, the numerical evaluation of $\tilde{\Psi}$ given in (13) is now discussed, starting by defining the following 3D arrays:

$$\begin{aligned} \psi &\equiv \{\psi(\Lambda, \mathbf{n})\} \in \mathbb{C}^{N_2 \times N_1 \times N_3}, \\ \tilde{\Psi} &\equiv \{\tilde{\Psi}(\Lambda, \mathbf{m})\} \in \mathbb{C}^{N_2 \times N_1 \times N_3}, \\ \mu &\equiv \{\exp(i2\pi R m_3 n_2), \forall n_1\} \in \mathbb{C}^{N_2 \times N_1 \times N_3}, \end{aligned} \quad (18)$$

where $R = \delta_{r_2} \delta_{q_3} \sin \theta_B$. Numerical implementation of (13) would then take the following form:

$$\tilde{\Psi} = \mathbf{DFT}_{\perp}[\mathbf{DFT}_3(\psi) \odot \mu] \delta_r \cos \theta_B. \quad (19)$$

Here, \mathbf{DFT}_3 is a 1D DFT operator that acts along the third dimension of a 3D array, and \mathbf{DFT}_{\perp} is a 2D DFT operator acting along the two other array dimensions. The ‘ \odot ’ symbol represents component-wise multiplication between matrices, and $\delta_r \equiv \delta_{r_1} \delta_{r_2} \delta_{r_3}$ is the real-space voxel volume. The conjugate operation to (19), derived from (14), would then read

$$\psi = \mathbf{IDFT}_3[\mathbf{IDFT}_{\perp}(\tilde{\Psi}) \odot \mu^*] \frac{1}{\delta_r \cos \theta_B}, \quad (20)$$

where \mathbf{IDFT}_3 and \mathbf{IDFT}_{\perp} are the inverse of the DFT operators introduced above and ‘ $*$ ’ denotes a component-wise complex-conjugate operation.

The role of μ in the transformations (19) and (20) is actually to produce an implicit interpolation in order to appropriately ‘shear’ (‘unshear’) Fourier space to conform to the detection geometry as dictated by the experiment. However, no interpolation error should arise from this strategy as it relies on an artifact-free sub-pixel shifting operation. We demonstrate the effectiveness of utilizing the specialized discrete Fourier transformations proposed in this section with a numerical phase-retrieval problem depicted in Fig. 3. Featured is a reconstruction result obtained by employing the popular and well known iterative error reduction (ER) phase-retrieval strategy for 3D BCDI adapted with the above transformations. To aid in implementing this approach, we provide in Appendix B the MATLAB code that implements this strategy for ER.

Finally, we point out that the sampling rates in (15) and (16) should define orthogonal meshes that are consistent with the (non-orthogonal) experimental sampling mesh. This issue is fully addressed in the next subsection.

3.3. Orthogonal direct and reciprocal meshes versus experimental mesh

Let us denote by $\delta_{\tilde{q}_1}$ and $\delta_{\tilde{q}_2}$ the experimental sampling rates in the detector plane ($\tilde{\mathbf{k}}_1, \tilde{\mathbf{k}}_2$) and by $\delta_{\tilde{q}_3}$ the experimental sampling rates along the rocking-curve direction $\tilde{\mathbf{k}}_3$. Those sampling rates are assumed to be appropriately set by the user² and serve as a reference for the setting of the ‘orthogonal’ sampling rates δ_{q_1} , δ_{q_2} and δ_{q_3} defined in (16). In particular, because we chose the orthogonal and the non-orthogonal frames such that $\mathbf{k}_1 = \tilde{\mathbf{k}}_1$ and $\mathbf{k}_2 = \tilde{\mathbf{k}}_2$ (see Fig. 2), we need $\delta_{q_1} = \delta_{\tilde{q}_1}$ and $\delta_{q_2} = \delta_{\tilde{q}_2}$, which can be derived in a straightforward way, as would be done for a standard transmission-geometry CDI experiment:

$$\delta_{q_1} \equiv \delta_{q_2} = \frac{1}{\lambda} \frac{p}{D}, \quad (21)$$

with (as in Part I) λ the X-ray wavelength, D the sample-to-detector distance and p the pixel pitch of the camera. The

² The sampling rates in the non-orthogonal frame ($\tilde{\mathbf{k}}_1, \tilde{\mathbf{k}}_2, \tilde{\mathbf{k}}_3$) are usually defined in order to comply with the ‘oversampling criterion’, which ensures (from the Shannon–Nyquist sampling theorem) that no information is lost during the experimental sampling (Sayre, 1952).

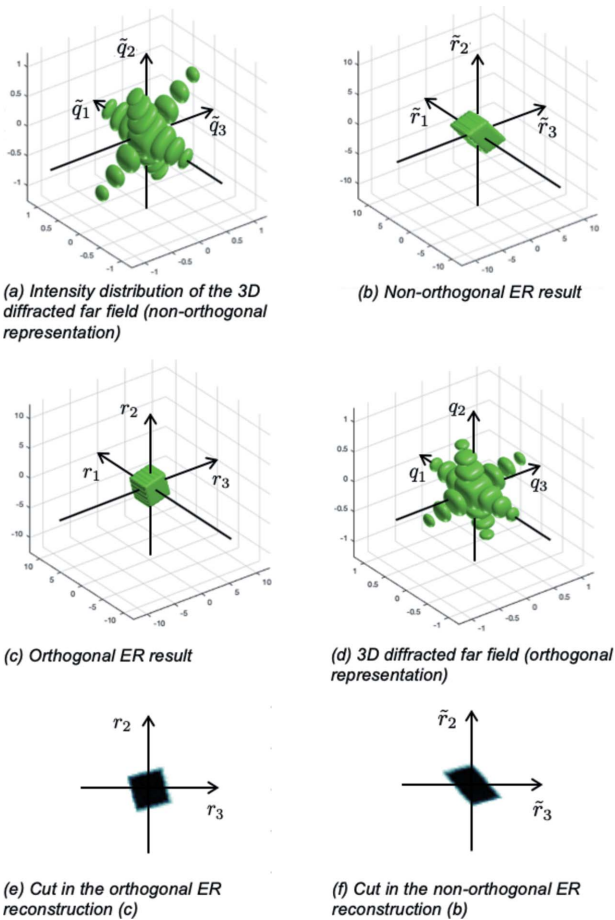


Figure 3 Reconstruction of a uniform real-valued cubic sample from the intensity of the 3D diffracted field measured along the RC. (a) The stack of noise-free intensity patterns collected along the RC is identical to the intensity of the non-orthogonal representation of the 3D diffracted field $\tilde{\Psi}$. (b) From these noise-free measurements, the sample estimate provided with the standard ER iteration is retrieved in a non-orthogonal frame, hence producing geometrical distortions of the cubic sample. In contrast, the modified ER algorithm (given in Appendix B) provides an orthogonal representation for the sample estimate (c) and its 3D diffracted far field (d). The 2D cuts shown in (e) and (f) clearly illustrate the geometric sample distortion expected in processing the data with non-orthogonal geometries. The results shown in (b) and (c) are obtained with 100 iterations of ER with a perfect knowledge of the support of the sample, either in its non-orthogonal representation for (b) or in its orthogonal representation for (c). The mesh size is $N_1 \times N_2 \times N_3 = 250^3$ and the computational time per iteration with a regular laptop is 0.96 s for (b) and 1.3 s for (c).

sampling rate δ_{q_3} , acting along \mathbf{k}_3 , must be considered more carefully because the two frames differ only by $\mathbf{k}_3 \neq \tilde{\mathbf{k}}_3$, as seen in Fig. 2. The Fourier sampling increment expressed on the orthogonal basis is arrived upon by projecting the sampling increment $\delta_{\tilde{q}_3}$ from the non-orthogonal frame:

$$\delta_{q_3} = \delta_{\tilde{q}_3} \cos \theta_B. \quad (22)$$

Fig. 2 shows this relationship geometrically. We note that the expression for δ_{q_3} is not given in terms of more fundamental experimental parameters because it is dependent on the choice of angular increment that the experimenter implements in the rocking-curve measurement. A detailed discussion of how to derive δ_{q_3} in terms of these experimental parameters is given in Appendix A, and in Part I for the case of a more general diffraction geometry.

We consider next the derivation of $(\delta_{r_1}, \delta_{r_2}, \delta_{r_3})$, the sampling rates in orthogonal real space. They should comply first with constraint (17), with certain subtleties that should not be overlooked. It is useful then to consider the geometric

constructions presented in Fig. 4 as an aid in deriving these real-space sampling increments. In this figure, a 2D cut through synthetic BCDI data from a cubic sample is shown. In the Fourier domain shown in Fig. 4, the structure of the cube is encoded as a 2D sinc function diffraction intensity pattern. In each panel, the sinc function fringes are recognizable, but they manifest themselves in different ways by manipulating the basis vectors of the Fourier volume interrogated by the rocking curve. Manipulating these bases in a specific manner will enable us to define the real-space sampling increments needed in (15).

(1) In Fig. 4(a), the 2D sinc function is shown in the measurement frame, equivalent to the 3D ‘data stack’ from the rocking curve. The fringes of the 2D sinc function in this frame are clearly not perpendicular, and the fringe oscillation periods along the two primary axes of the cube are not the same. This distortion is due to the shear introduced by the inherently non-orthogonal nature of any rocking-curve measurement.

(2) Fig. 4(b) maps the data stack to a frame where the basis vectors $\tilde{\mathbf{k}}_2$ and $\tilde{\mathbf{k}}_3$ are non-orthogonal, to the degree dictated by the geometry of the experiment. In this frame, the fringes of the 2D sinc function are perpendicular and the oscillation periods along both fringe directions are the same. In this frame, we recognize the basic symmetry and orientation of the cube used to generate these data. What is now sheared is the volume of Fourier space $\Gamma_{\tilde{\Psi}}$ surveyed by the rocking curve. This representation is therefore useful, but it is built upon on a non-orthogonal Fourier basis that is not amenable to a description of orthogonal real-space sampling of the object.

(3) To alleviate this, we cast the rocking-curve volume onto an orthogonal Fourier basis, as shown in Fig. 4(c). In this frame, capturing all of the information contained in the rocking curve requires a rectangular area along the orthogonal basis vectors $\mathbf{k}_2, \mathbf{k}_3$. This rectangular Fourier-space domain, denoted as Γ_{Ψ} , will define the Fourier-space window used in an iterative phase-retrieval algorithm that enforces an orthogonal view of the sample. Thus a single 3D array of pixels should be defined that will be iteratively transformed from real to Fourier space and back over the course of phase retrieval. However, in imagining such an approach, a complication arises because the extent of Γ_{Ψ} along the q_2 direction, given by $(\Delta_{\tilde{q}_2} + \Delta_{\tilde{q}_3} \sin \theta_B)$ as

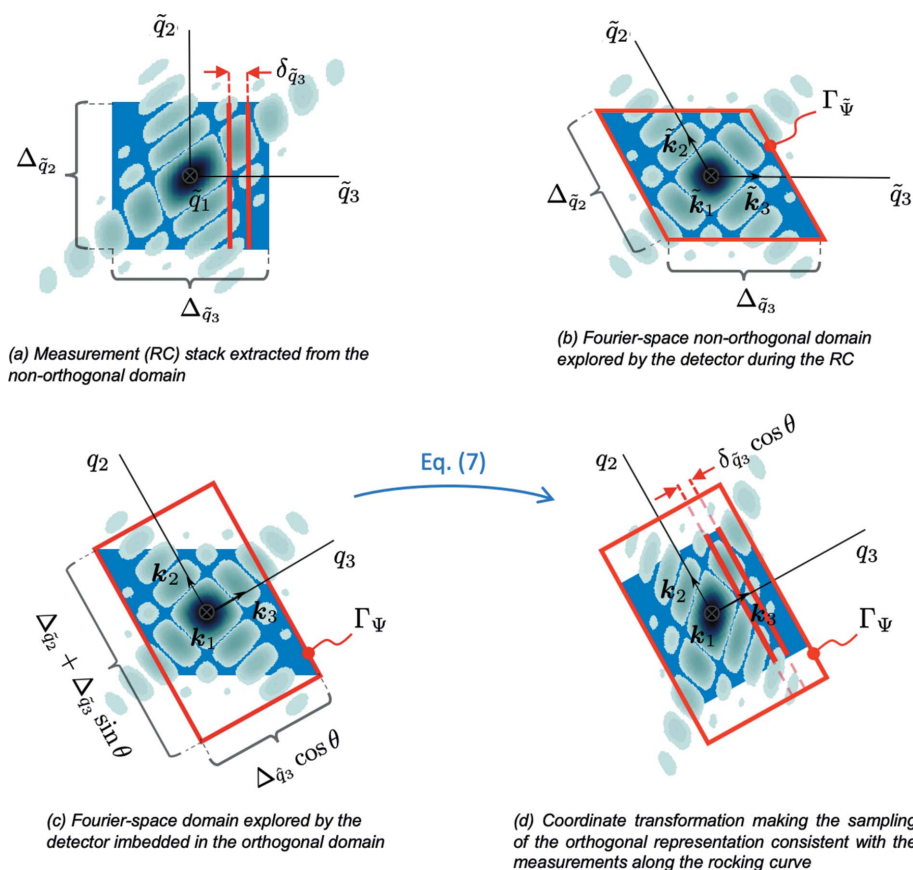


Figure 4

Non-orthogonal and orthogonal representations of the diffracted far field in the Bragg geometry. (a) The 3D stack of intensity measurements obtained during the RC, as stored in a 3D array, (b) is produced by the regular sampling of the far field Ψ performed within the non-orthogonal measurement domain imposed by the detector geometry and delimited by the shaded area $\Gamma_{\tilde{\Psi}}$. (c) In an orthogonal basis, the far field Ψ computed in a domain Γ_{Ψ} can be defined to contain the non-orthogonal domain $\Gamma_{\tilde{\Psi}}$. In addition, after the coordinate transformation given in (7), Ψ provides a computed representation of the far field whose sampling is totally consistent with the data (RC) stack (d). Because the non-orthogonal measurement domain $\Gamma_{\tilde{\Psi}}$ shown in (d) is smaller than Γ_{Ψ} , the computed representation of Ψ in Γ_{Ψ} is not totally constrained by the intensity measurements shown in (b). For the sake of the demonstration, a cubic sample has been numerically designed, with its Bragg vector pointing towards one of its edges. Note the agreement between (a) and (d).

shown visually in Fig. 4(c), is not necessarily divisible by δ_{q_2} , leading to a situation where N_2 is not an integer number of pixels. This can be addressed by simply rounding up so that the integer pixelation is enforced. Thus, we have $N_2 = \lceil (\Delta_{\tilde{q}_2} + \Delta_{\tilde{q}_3} \sin \theta_B) / \delta_{q_2} \rceil$, where $\lceil \cdot \rceil$ is a round-up operation. Numerically, this creates a domain that is slightly larger than Γ_ψ but that retains the important property that it still totally encapsulates the RC measurement volume. We note that a similar rounding consideration should also be made for N_1 if one considers more general nonsymmetric Bragg CDI measurements, but this is not necessary for the simpler geometry considered here.

Having arrived at a DFT-compatible description of Γ_ψ in Fig. 4(c), we can readily derive the corresponding real-space increments of the 3D pixel array. This is done by using the extent of the Fourier domain Γ_ψ to determine the magnitudes of the sampling rates along the three orthogonal directions in real space, which will generally all be different. In each of the orthogonal directions, we have

$$\delta_{r_3} = \frac{1}{\Delta_{\tilde{q}_3} \cos \theta_B}, \quad (23)$$

$$\delta_{r_1} = \frac{1}{\Delta_{\tilde{q}_1}} \quad \text{and} \quad \delta_{r_2} = \frac{1}{\delta_{q_2} \lceil (\Delta_{\tilde{q}_2} + \Delta_{\tilde{q}_3} \sin \theta_B) / \delta_{q_2} \rceil}. \quad (24)$$

In these relations, $\Delta_{\tilde{q}_3}$ is the extent of Γ_ψ along the rocking-curve direction $\tilde{\mathbf{k}}_3$, and $\Delta_{\tilde{q}_1}$ and $\Delta_{\tilde{q}_2}$ are the Fourier extents of the detector along $\tilde{\mathbf{k}}_1$ ($\equiv \mathbf{k}_1$) and $\tilde{\mathbf{k}}_2$ ($\equiv \mathbf{k}_2$), respectively. The case of δ_{r_2} is particularly interesting because it is derived from an edge length of Γ_ψ that exceeds the Fourier-space window subtended by the pixels of the detector. It is related to the total extent along \mathbf{k}_2 interrogated by the entire measurement within the orthogonal frame. Similarly, δ_{r_3} is determined by the height of the parallelogram rather than the rocking-curve extent in the original measurement frame. These derivations build a stronger connection with the details of the physical experiment and are not readily apparent when only considering the ‘sheared’ measurement domain Γ_ψ shown in Fig. 4(b).

The discussion above sets the orthogonal meshing in both the real and the Fourier spaces so that it is consistent with the non-orthogonal experimental sampling. The numerical relations (19) and (20) are then the means by which to design a phase-retrieval algorithm in which the sample frame is orthogonal. In particular, (19) transforms the far field computed in an orthogonal real-space domain Γ_ψ so that it matches with the RC intensity measurements: as shown in Fig. 4(d), the resulting geometric shear yields a description of the far field that closely matches Fig. 4(a), in that the fringes of the sinc function are no longer perpendicular and they are unevenly spaced. As a consequence, relation (19) can be used within a 3D BCDI phase-retrieval strategy to enforce a ‘data constraint’ or ‘modulus constraint’ for each iteration that is mapped to orthogonal real space *via* (20). It should also be noted that, in imposing such a modulus constraint, some sample points of the numerical array will not be constrained

by intensity measurements of the RC because of our construction of Γ_ψ . Generally, this is not a concern because phase-retrieval algorithms can be designed to handle a set of ‘missing’ or ‘floating’ data points (Nishino *et al.*, 2003; Marchesini *et al.*, 2003; Berenguer *et al.*, 2013).

The resulting numerical processing of experimental data is then very efficient thanks to the transforms (19) and (20). However, it should be stressed that these transformations can only be derived when the rocking curve is evenly sampled. With irregular rocking curves, we shall resort to another (computationally less attractive) strategy that is fully described in the next section.

4. Alternative BCDI mappings *via* projections and back-projections

As we show below, continuous FT/IFT operators can also be interpreted as projection and back-projection operations, consistent with the Fourier slice projection theorem. This interpretation provides the means by which to devise a second strategy to link either $\tilde{\psi}$ or ψ to the ‘measurement space’ $\tilde{\Psi}$ with even greater flexibility. This flexibility offers the possibility to account for more complex physical models of the system. For example, the requirement that a rocking curve be measured with evenly spaced angular increments can be relaxed with this approach. We note that the flexibility of this back-projection approach has been employed in several recent studies as a means to solve specific problems within BCDI and Bragg ptychography that required the incorporation of more physically realistic models of the experiment to enable new types of measurements. Examples include determination of the angular errors of a BCDI rocking curve (Calvo-Almazán *et al.*, 2019), accounting for Fourier-space scaling in a BCDI energy-scanning measurement (Cha *et al.*, 2016), dealing with raster grid misregistry in 3D Bragg ptychography (Hill *et al.*, 2018) and enabling 3D reconstructions from 2D Bragg ptychography data measured at a fixed angle (Hruszkewycz *et al.*, 2017). Though the approach has been used effectively in different contexts in the literature, a consolidated mathematical derivation and roadmap for numerical implementation is lacking. Thus, the goal of this section is to derive the relevant relationships and strategies for their numerical evaluation *via* DFT/IDFT to facilitate the adoption of this concept towards yet more BCDI applications.

4.1. Mappings between non-orthogonal representations

A general property of an n -dimensional FT operator, regardless of the representation frame, is that it can be implemented as a series of lower-dimensional FTs, a fact we will take advantage of in this section. We start by considering the Fourier pair in the ‘non-orthogonal’ representation $\tilde{\psi} \rightleftharpoons \tilde{\Psi}$:

$$\tilde{\Psi} = \mathcal{F} \tilde{\psi} = \mathcal{F}_\perp \mathcal{F}_3 \tilde{\psi}. \quad (25)$$

We next define a notation to designate a single 2D slice in the measurement frame that corresponds to a given angle that

might be interrogated by a rocking curve. This could be a Fourier-space coordinate that is one of a series of regular rocking-curve intervals, but it need not be. The notation we adopt is that $\tilde{q}_{3;0}$ represents an arbitrary point along the \tilde{q}_3 measurement axis. At the point $\tilde{q}_{3;0}$, we expect that a 2D cut of the far-field pattern could be expressed as

$$\tilde{\Psi}_{\perp; \tilde{q}_{3;0}}(\tilde{\mathbf{q}}_{\perp}) := \tilde{\Psi}(\tilde{\mathbf{q}}_{\perp}, \tilde{q}_3 = \tilde{q}_{3;0}) = \int_{\mathbb{R}^3} \tilde{\psi}(\tilde{\mathbf{r}}) \exp[-i2\pi(\tilde{r}_1\tilde{q}_1 + \tilde{r}_2\tilde{q}_2 + \tilde{r}_3\tilde{q}_{3;0})] d\tilde{\mathbf{r}}. \quad (26)$$

Alternatively, the integral above can be rearranged so that this 2D cut $\tilde{\Psi}_{\perp; \tilde{q}_{3;0}}$ is obtained *via* the 2D Fourier transform of a specific 2D projection of the diffracting object:

$$\tilde{\Psi}_{\perp; \tilde{q}_{3;0}} = \mathcal{F}_{\perp} \tilde{\psi}_{\perp; \tilde{q}_{3;0}}. \quad (27)$$

In this equation, we introduce a new 2D function $\tilde{\psi}_{\perp; \tilde{q}_{3;0}}$ that represents the appropriate projection of the 3D object needed to produce a specific cut along the rocking curve of the measurement-frame diffraction pattern. It is given by

$$\tilde{\psi}_{\perp; \tilde{q}_{3;0}}(\tilde{\mathbf{r}}_{\perp}) := \int_{\mathbb{R}} \tilde{\psi}(\tilde{\mathbf{r}}) \exp(-i2\pi\tilde{r}_3\tilde{q}_{3;0}) d\tilde{r}_3. \quad (28)$$

Central to this projection is the fact that the 3D object is to be multiplied by a complex exponential that imparts an oscillating, spatially modulated phase on the object. The period of this phase oscillation encodes the real-space spatial frequency along \tilde{r}_3 that corresponds to the desired cut of the Fourier-space diffraction pattern at $\tilde{q}_{3;0}$. Thus, (27) provides a forward mapping $\tilde{\psi} \rightarrow \tilde{\Psi}$ in which a full 3D Fourier-space description of $\tilde{\Psi}$ can be built up slice-by-slice by invoking a series of 2D Fourier transformations upon specific projections of the object that include appropriate phase modulation.

Conversely, the complimentary backwards transformation $\tilde{\Psi} \rightarrow \tilde{\psi}$ can also be derived by a similar construction. We first consider the result of a 3D inverse Fourier transform acting upon a single 2D slice of the far-field diffraction. Because only a 2D slice of the 3D far field is input in this transformation, we do not expect the resulting real-space description of the object to be complete. Thus, we designate the quantity $\tilde{\psi}_{\tilde{q}_{3;0}}(\tilde{\mathbf{r}})$ to represent the 3D description of the object consistent with the information contained in the $\tilde{\Psi}_{\perp; \tilde{q}_{3;0}}$ slice:

$$\begin{aligned} \tilde{\psi}_{\tilde{q}_{3;0}}(\tilde{\mathbf{r}}) &:= \int_{\mathbb{R}^3} \tilde{\Psi}_{\perp; \tilde{q}_{3;0}}(\tilde{\mathbf{q}}_{\perp}) \delta(\tilde{q}_3 - \tilde{q}_{3;0}) \exp(i2\pi\tilde{\mathbf{r}}^T\tilde{\mathbf{q}}) d\tilde{\mathbf{q}} \\ &= \exp(i2\pi\tilde{r}_3\tilde{q}_{3;0}) [\mathcal{F}_{\perp}^{-1} \tilde{\Psi}_{\perp; \tilde{q}_{3;0}}](\tilde{\mathbf{r}}_{\perp}) \\ &= \exp(i2\pi\tilde{r}_3\tilde{q}_{3;0}) \tilde{\psi}_{\perp; \tilde{q}_{3;0}}(\tilde{\mathbf{r}}_{\perp}), \end{aligned} \quad (29)$$

where δ is the Dirac distribution. To obtain a complete description of the object $\tilde{\psi}(\tilde{\mathbf{r}})$, we must integrate over all of the possible $\tilde{\psi}_{\tilde{q}_{3;0}}(\tilde{\mathbf{r}})$ that correspond to the continuum of available slices of a far-field diffraction pattern:

$$\tilde{\psi}(\tilde{\mathbf{r}}) = \int_{\mathbb{R}} \tilde{\psi}_{\tilde{q}_{3;0}}(\tilde{\mathbf{r}}) d\tilde{q}_{3;0}. \quad (30)$$

We note that (29) represents a back-projection that acts as a complimentary operation to the projection in (28). As in the case of the projection, the back-projection takes on a specific

nature with regard to the phases of the real-space description of the object. We find that the 3D quantity $\tilde{\psi}_{\tilde{q}_{3;0}}$ is composed of the 2D field $\tilde{\psi}_{\perp; \tilde{q}_{3;0}}$ that is self-similar along the direction \tilde{r}_3 , but for a spatially modulated phase. The two phase modulation terms associated with projection in the forward transformation and with back-projection in the backward transformation are simply related complex conjugates because they factor out of the forward and inverse Fourier integrals, respectively. This particular construction of Fourier transformations emphasizes the ‘slice-by-slice’ nature of the measurement rather than treating the rocking curve as an explicitly 3D interrogation of Fourier space. This emphasis provides substantially more flexibility. For example, with the projection/back-projection framework, appropriate transformations can easily be designed to account for data measured at arbitrary or irregular angles along a rocking curve. Additionally, with this mapping from a non-orthogonal description of the far field $\tilde{\Psi}$ to an orthogonal real-space description of the sample ψ is also possible, as we show below.

4.2. Linking orthogonal real space and non-orthogonal measurement space via projections and back-projections

Projection and back-projection also provide a convenient way to compute the ‘non-orthogonal’ representation $\tilde{\Psi}$ from the real-space ‘orthogonal’ representation ψ , and *vice versa*. We first consider the reciprocal-space displacement that is needed from the center of the diffraction pattern to extract our slice of interest $\tilde{\Psi}_{\perp; \tilde{q}_{3;0}}$. This displacement vector, or shift vector, is to be determined in the orthogonal \mathbf{q} frame. For the case of symmetric two-circle diffraction considered here, the three coordinates of the shift vector as expressed in the orthogonal frame are

$$\begin{aligned} \Delta_{\tilde{q}_{3;0}} &= \tilde{q}_{3;0} \cos \theta_B [0 \quad -\tan \theta_B \quad 1]^T \\ &= [0 \quad -\tilde{q}_{3;0} \sin \theta_B \quad \tilde{q}_{3;0} \cos \theta_B]^T. \end{aligned} \quad (31)$$

The geometry of this shift vector is consistent with the means of deriving Γ_{ψ} earlier, as shown in Fig. 4.

This shift vector can now be used in combination with equation (7) in order to map the Fourier-space measurement frame to an orthogonal one:

$$\tilde{\Psi}_{\perp; \tilde{q}_{3;0}}(\tilde{\mathbf{q}}_{\perp}) = \cos \theta_B \Psi(\mathbf{q} + \Delta_{\tilde{q}_{3;0}})|_{\mathbf{q}_{\perp} = \tilde{\mathbf{q}}_{\perp}, q_3 = 0}. \quad (32)$$

As above, we note that a given slice of the far-field pattern $\tilde{\Psi}_{\perp; \tilde{q}_{3;0}}(\tilde{\mathbf{q}}_{\perp})$ is related to a Fourier transform of a projection of the object subject to specific phase modulation. This also holds true when describing the object in an orthogonal frame, so long as the appropriate shift vector (expressed in the dual orthogonal Fourier frame) is used to determine the phase modulation term. So, we define the following quantity:

$$\psi_{\perp; \Delta_{\tilde{q}_{3;0}}}(\mathbf{r}_{\perp}) := \cos \theta_B \int_{\mathbb{R}} \psi(\mathbf{r}) \exp(-i2\pi\mathbf{r}^T\Delta_{\tilde{q}_{3;0}}) dr_3, \quad (33)$$

such that

$$\tilde{\Psi}_{\perp; \tilde{q}_{3;0}}(\tilde{\mathbf{q}}_{\perp}) = [\mathcal{F}_{\perp} \psi_{\perp; \Delta_{\tilde{q}_{3;0}}}] (\mathbf{q}_{\perp} = \tilde{\mathbf{q}}_{\perp}). \quad (34)$$

There is a parallel to be drawn between $\psi_{\perp; \Delta \tilde{q}_{3;0}}$ and the intermediate functions ξ and ζ from Section 3.1. These functions are constructed in a way to rectify the difference between orthogonal and non-orthogonal conjugate frames by utilizing spatially varying phase terms. They are also constructed such that the details of accounting for the skewed RC measurement axis are separated from the \mathbf{q}_{\perp} and \mathbf{r}_{\perp} coordinates such that a 2D Fourier transformation can be deployed.³

We can also derive the series of backward operations that constructs ψ from $\tilde{\Psi}$. The derivation is based on equation (30) used in combination with the fact (from Section 2) that $\psi(\mathbf{r}) \equiv \tilde{\psi}(\tilde{\mathbf{r}} = \mathbf{B}^{-1}\mathbf{r})$ with $\mathbf{B}^{-1} = \mathbf{B}_q^T$. We start by recasting the result of back-projection from a single slice of the diffraction field from the measurement frame into the orthogonal sample frame:

$$\begin{aligned} \psi_{\tilde{q}_{3;0}}(\mathbf{r}) &:= \tilde{\psi}_{\tilde{q}_{3;0}}(\tilde{\mathbf{r}} = \mathbf{B}^{-1}\mathbf{r}) \\ &= \exp(i2\pi\mathbf{r}^T \Delta_{\tilde{q}_{3;0}}) [\mathcal{F}_{\perp}^{-1} \tilde{\Psi}_{\perp; \tilde{q}_{3;0}}](\mathbf{r}_{\perp}). \end{aligned} \tag{35}$$

As before, the information regarding the degree of shear of the rocking curve is included in the complex exponential term. This leads us again to an expression in which the orthogonal description of the sample can be obtained by integrating over all possible diffraction pattern slices available in the measurement frame:

$$\psi(\mathbf{r}) := \tilde{\psi}(\mathbf{B}^{-1}\mathbf{r}) = \int_{\mathbb{R}} \psi_{\tilde{q}_{3;0}}(\mathbf{r}) d\tilde{q}_{3;0}. \tag{36}$$

Equations (34) and (36) are the main results of this subsection. These equations link any ‘slice’ in $\tilde{\Psi}$ with the orthogonal real-space representation ψ . Thus, these two equations can be utilized within a phase-retrieval algorithm to directly update an orthogonal real-space representation regardless of the order or regularity with which the slices were measured experimentally.

To illustrate some of the concepts and relationships of the projection/back-projection approach, we refer to Fig. 5. Panel (a) shows a cubic crystal expressed in two frames corresponding to the real-space conjugate measurement frame $\tilde{\mathbf{e}}$

³ Because we have $\tilde{\mathbf{r}} = \mathbf{B}^{-1}\mathbf{r}$ with $\mathbf{B}^{-1} = \mathbf{B}_q^T$, we can show from (6) that $\tilde{\mathbf{r}}_{\perp} = \mathbf{r}_{\perp}$. This result means that the ‘projected exit fields’ $\psi_{\perp; \Delta \tilde{q}_{3;0}}$ and $\tilde{\psi}_{\tilde{q}_{3;0}}$ given in (33) and (28), respectively, are in fact identical mathematical expressions.

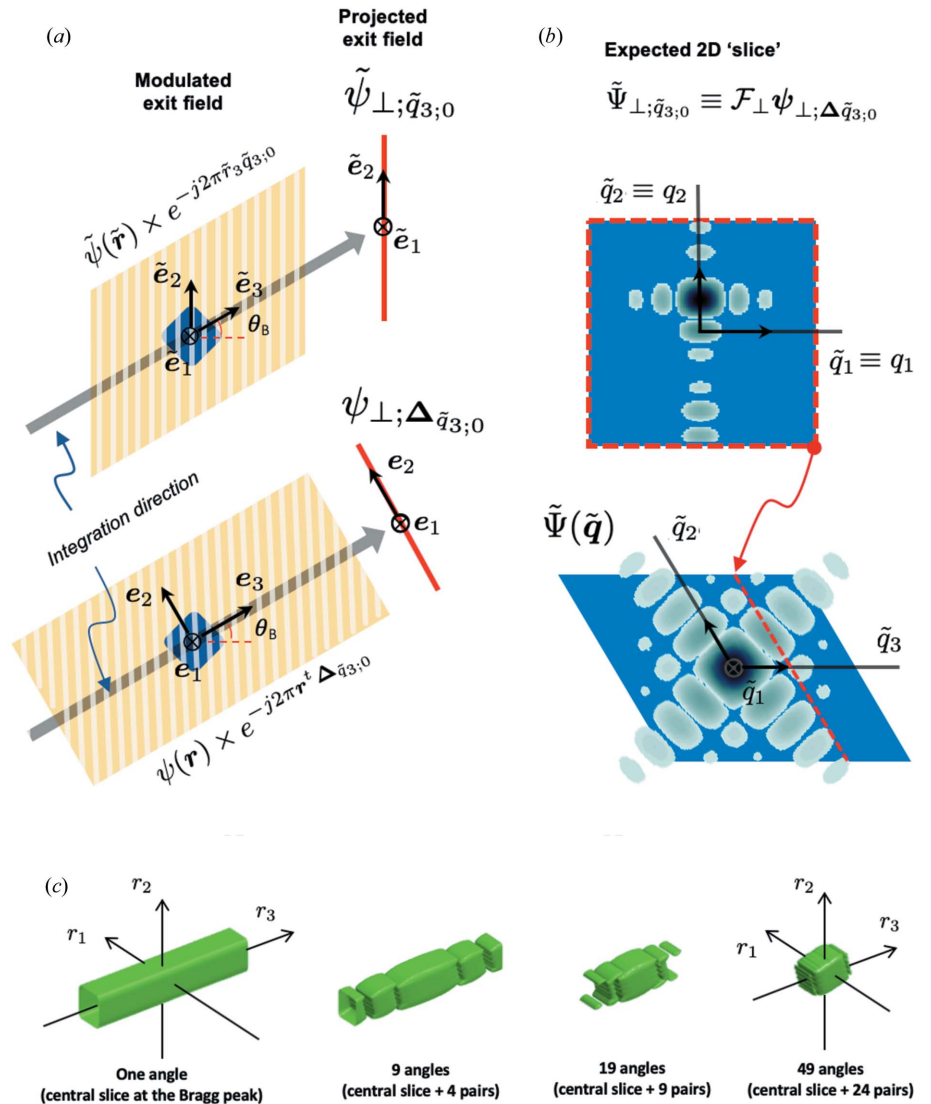


Figure 5 Illustration of the projection/back-projection strategy. (a) The integrated exit field in the non-orthogonal or in the orthogonal real-space representation allows us to derive (b) a ‘slice’ $\tilde{\Psi}_{\perp; \tilde{q}_{3;0}}$ extracted from $\tilde{\Psi}(\tilde{\mathbf{q}})$ at $\tilde{q}_3 = \tilde{q}_{3;0}$. (c) Conversely, the summation of a series of back-projections allows us to retrieve the object from its evenly sampled ‘slices’; here, the retrieved sample is converging toward the cubic real-valued particle shown in Fig. 3.

and the orthogonal sample frame \mathbf{e} . As described by equations (28) and (33), a different phase modulation term should be applied in each frame. These phase modulations are represented in the figure by the white/yellow stripes, and we find that they manifest themselves differently with respect to the two frames, but they both encode equivalent information. Thus, applying the integration along $\tilde{\mathbf{e}}_3$ or \mathbf{e}_3 , respectively, produces 2D exit wavefields that are the same. Applying a 2D Fourier transform to the resulting projected exit field will produce the far-field diffraction pattern shown in Fig. 5(b). This diffraction pattern corresponds to a slice of the overall 3D Fourier far-field diffraction that is offset from the center by a desired amount along \tilde{q}_3 . The inverse process of constructing a description of the object ψ from a series of back-projections corresponding to a set of $\tilde{\Psi}$ is shown in Fig. 5(c). From a single

slice, only the outline of the cube can be discerned. However, as real-space back-projections from an increasing number of Fourier slices are integrated, the form of the cube takes shape. In the next section, we derive convenient means of numerically implementing these relations.

4.3. Numerical evaluation with digital Fourier transforms

The numerical implementation of mapping between non-orthogonal representation spaces presented in Section 4.1 is considered first. We note that the discussion presented here relies on some of the notation introduced in Section 3.2. Let us introduce $\tilde{\psi} \in \mathbb{C}^{N_2 \times N_1 \times N_3}$ as the 3D array built from the regular spatial sampling of ψ and $\tilde{\Psi}_{\perp; \tilde{q}_{3;0}} \in \mathbb{C}^{N_2 \times N_1}$ as the 2D array built from the regular sampling of the detector plane ($\tilde{\mathbf{q}}_{\perp}$) at $\tilde{q}_3 = \tilde{q}_{3;0}$. We deduce from (27) the discretized form of the relationship:

$$\tilde{\Psi}_{\perp; \tilde{q}_{3;0}} = \mathbf{DFT}_{\perp}[\mathbf{SUM}_3(\tilde{\psi} \odot \tilde{\mu}_{\tilde{q}_{3;0}})]\delta_{\tilde{r}}, \quad (37)$$

where $\delta_{\tilde{r}} \equiv \delta_{\tilde{r}_1} \delta_{\tilde{r}_2} \delta_{\tilde{r}_3}$ is the voxel volume in the non-orthogonal frame ($\tilde{\mathbf{e}}_1, \tilde{\mathbf{e}}_2, \tilde{\mathbf{e}}_3$) and \mathbf{SUM}_3 is a summation (*i.e.* a projection) operator acting along the third dimension of the 3D array. The array describing the phase modulation needed to produce the desired ‘slice’ $\tilde{q}_3 = \tilde{q}_{3;0}$ is given by

$$\tilde{\mu}_{\tilde{q}_{3;0}} \equiv \{\exp(-i2\pi n_3 \delta_{\tilde{r}_3} \tilde{q}_{3;0}), \forall(n_1, n_2)\} \in \mathbb{C}^{N_2 \times N_1 \times N_3}. \quad (38)$$

Conversely, the numerical implementation of the back-projection step (29) is given by

$$\tilde{\psi}_{\tilde{q}_{3;0}} = \tilde{\mu}_{\tilde{q}_{3;0}}^* \odot \mathbf{REP}_3[\mathbf{DFT}_{\perp}^{-1}(\tilde{\Psi}_{\perp; \tilde{q}_{3;0}})]\frac{1}{\delta_{\tilde{r}_1} \delta_{\tilde{r}_2}}. \quad (39)$$

In this expression, \mathbf{REP}_3 is a replication (*i.e.* a back-projection) operator that creates an $N_2 \times N_1 \times N_3$ array from an $N_2 \times N_1$ array, ensuring that the array is self-similar along N_3 . In the back-projection step, the phase-modulation term is the complex conjugate (*) of $\tilde{\mu}_{\tilde{q}_{3;0}}$.

The sampling along the RC implies that a set of ‘slices’ $\tilde{\Psi} \equiv \{\tilde{\Psi}_{\perp; \tilde{q}_3} \mid \tilde{q}_3 = \tilde{q}_{3;0}, \dots, \tilde{q}_{3;N_3-1}\}$ should be computed to provide the expected measurements that will be eventually constrained by the data during phase retrieval. However, if we consider the case when the RC is regularly sampled then the regularity of the mesh along $\tilde{\mathbf{k}}_3$ allows one to sidestep the slice-by-slice approach and simply obtain all the slices with a single, much faster, 3D DFT: $\tilde{\Psi} = \mathbf{DFT}(\tilde{\psi})$. As a result, the projection/back-projection strategy described here will be appealing in situations, for example, when \tilde{q}_3 is unevenly sampled, as was demonstrated by Calvo-Almazán *et al.* (2019).

We now consider the numerical implementation of the projection/back-projection approach in mapping from an orthogonal sample space to a sheared measurement space and back. Starting from the orthogonal representation ψ , we deduce from (34) that a given far-field diffraction slice can be obtained numerically by

$$\tilde{\Psi}_{\perp; \tilde{q}_{3;0}} = \mathbf{DFT}_{\perp}[\mathbf{SUM}_3(\psi \odot \mu_{\tilde{q}_{3;0}})]\delta_{\tilde{r}} \cos \theta_B. \quad (40)$$

In this expression, $\psi \in \mathbb{C}^{N_2 \times N_1 \times N_3}$ is the 3D array built from the regular sampling of the orthogonal real-space sample representation, and

$$\mu_{\tilde{q}_{3;0}} \equiv \{\exp(-i2\pi \mathbf{n}^T \Lambda_r \Delta_{\tilde{q}_{3;0}})\} \in \mathbb{C}^{N_2 \times N_1 \times N_3} \quad (41)$$

is the phase-modulation array (the notations \mathbf{n} and Λ_r were introduced in Section 3.3). Conversely, the numerical implementation of the back-projection step (35) is given by

$$\psi_{\tilde{q}_{3;0}} = \mu_{\tilde{q}_{3;0}}^* \odot \mathbf{REP}_3[\mathbf{DFT}_{\perp}^{-1}(\tilde{\Psi}_{\perp; \tilde{q}_{3;0}})]\frac{1}{\delta_{\tilde{r}_1} \delta_{\tilde{r}_2} \cos \theta_B}. \quad (42)$$

Following (35), the real-space back-projections corresponding to a set of individual ‘slices’ can be summed to provide an estimate of the diffracting sample:

$$\psi \simeq \sum_{n=0}^{N_3-1} \psi_{\tilde{q}_{3;n}} \frac{1}{N_3 \delta_{\tilde{r}_3}}. \quad (43)$$

We note that equations (40) and (42) can be used as flexible building blocks by which to design new phase-retrieval reconstruction algorithms, as has been recently shown (Hruszkewycz *et al.*, 2017; Hill *et al.*, 2018; Calvo-Almazán *et al.*, 2019). As an aid to interested readers, an example of MATLAB code for such an algorithm is provided in Appendix B, in which the projection/back-projection strategy is implemented for the BCDI-ER phase-retrieval algorithm.

From a computational perspective, we point out that the increased adaptability of the projection/back-projection approach does come at a price regarding computation speed. If we consider the situations in which slices are regularly sampled along the RC direction then the repeated calculation of projection/back-projection over a regular mesh along \tilde{q}_3 is likely to be much slower than the 3D DFTs involved in (19). This is evident by noting that the run time of the ER phase-retrieval code of the 3D DFT method (given in Fig. 7; see Appendix B) is ten times faster than that for projection/back-projection (Fig. 8).

5. Conclusion

Bragg CDI provides the ability to measure a volume of Fourier space containing rich structural information about a Bragg-diffracting sample and to invert this measurement into a real-space image. The nature of the measurement is such that parallel sequential slices of Fourier space are obtained, which allows for the efficient and robust design of phase-retrieval algorithms for this purpose. However, using currently available phase-retrieval tools, Bragg CDI reconstructions exhibit geometric distortions induced by the non-orthogonal nature of the measurement in Fourier space. Although well understood, these distortions are a serious hurdle for the interpretation of the raw reconstruction.

In this two-part series, we provide a mathematically comprehensive view of this problem, and we outline several strategies aimed at addressing the issue in different ways. In Part I, we derive the means by which to transform the final raw BCDI reconstruction so that it can be displayed within an

arbitrary orthogonal real-space frame. This approach is currently in use in the BCDI community, and we provide in Part I the mathematical underpinnings of the method that will facilitate its adoption at a broader range of synchrotron beamlines. Part II addresses the problem from a different viewpoint. We aimed to develop Fourier transformations that were designed to reconcile the non-orthogonal frame of the measurement with an orthogonal representation of the sample. In this spirit, we derive two different transformations that achieve this for the case of regularly sampled and irregularly sampled experimental datasets. Importantly, these transformations can be embedded within the iterative loops of popular BCDI phase-retrieval routines, so that a natural orthogonal sample frame is built into the phase-retrieval framework *a priori*. This is tremendously advantageous when incorporating physical constraints that stem from the experimental geometry into the design of a phase-retrieval algorithm. Thus, the work presented in Parts I and II together provides a unified set of concepts for the BCDI community to address issues related to achieving natural 3D reconstruction representation and, more broadly, to embed these concepts more deeply into phase retrieval in order to enable the design of new types of BCDI experiments that cannot be realized with current methods.

APPENDIX A

Extension to arbitrary non-specular Bragg reflections

In most BCDI diffraction configurations, the ‘orthogonal’ Fourier-space frame $(\mathbf{k}_1, \mathbf{k}_2, \mathbf{k}_3)$ can be chosen such that $\mathbf{k}_\perp \equiv (\mathbf{k}_1, \mathbf{k}_2)$ is identical to the pair $\tilde{\mathbf{k}}_\perp \equiv (\tilde{\mathbf{k}}_1, \tilde{\mathbf{k}}_2)$ that corresponds to the detection plane. As a consequence, a general form for the transformation matrix (6) linking Ψ and $\tilde{\Psi}$ is

$$\mathbf{B}_q = \begin{bmatrix} 1 & 0 & | \\ 0 & 1 & | \mathbf{b} \\ 0 & 0 & | \end{bmatrix}. \tag{44}$$

In this expression, $\mathbf{b} \in \mathbb{R}^3$ is the decomposition of $\tilde{\mathbf{k}}_3$ in the ‘orthogonal’ basis $(\mathbf{k}_1, \mathbf{k}_2, \mathbf{k}_3)$. The specific expression of \mathbf{b} varies significantly in practice because it depends on the specific design of the diffractometer used in the measurement and on the nature of the scan. One such example is given in Section 4 in the Part I companion paper. The transformations presented in Sections 3 and 4 of the present paper are nevertheless easy to adapt to accommodate the generic form in (44).

First, let us consider the main results in Section 4. The relations (34), (35), (40) and (42) hold under the adaptation considered here, provided that the Fourier-space shift introduced in (31) obeys

$$\Delta_{\tilde{q}_{3,0}} = \tilde{q}_{3,0} \mathbf{b}. \tag{45}$$

We specify that the form of \mathbf{b} is the following, conforming to the convention presented in Section 3:

$$\mathbf{b} = [-b_1 \quad -b_2 \quad b_3]^T. \tag{46}$$

Then, the expression for the ‘forward’ step $\psi \rightarrow \tilde{\Psi}$ in the more general diffraction geometry in the continuous domain [analogous to relation (10)] will be as follows:

$$\tilde{\Psi}(\tilde{\mathbf{q}}) := b_3 [\mathcal{F}_\perp \xi](\tilde{\mathbf{q}}_\perp, b_3 \tilde{q}_3) \tag{47}$$

with

$$\xi(\mathbf{r}_\perp, q_3) := [\mathcal{F}_3 \psi](\mathbf{r}_\perp, q_3) \exp[i2\pi(\tilde{b}_1 r_1 + \tilde{b}_2 r_2) q_3], \tag{48}$$

where $\tilde{b}_1 \equiv b_1/b_3$ and $\tilde{b}_2 \equiv b_2/b_3$. We can also update the counterpart expression in the discrete domain [analogous to (19)]:

$$\tilde{\Psi} = \mathbf{DFT}_\perp [\mathbf{DFT}_x(\psi) \odot \mu] b_3 \delta_r, \tag{49}$$

with

$$\mu := \{\exp[i2\pi(n_1 \delta_{r_1} \tilde{b}_1 + n_2 \delta_{r_2} \tilde{b}_2) m_3 \delta_{q_3} b_3]\} \tag{50}$$

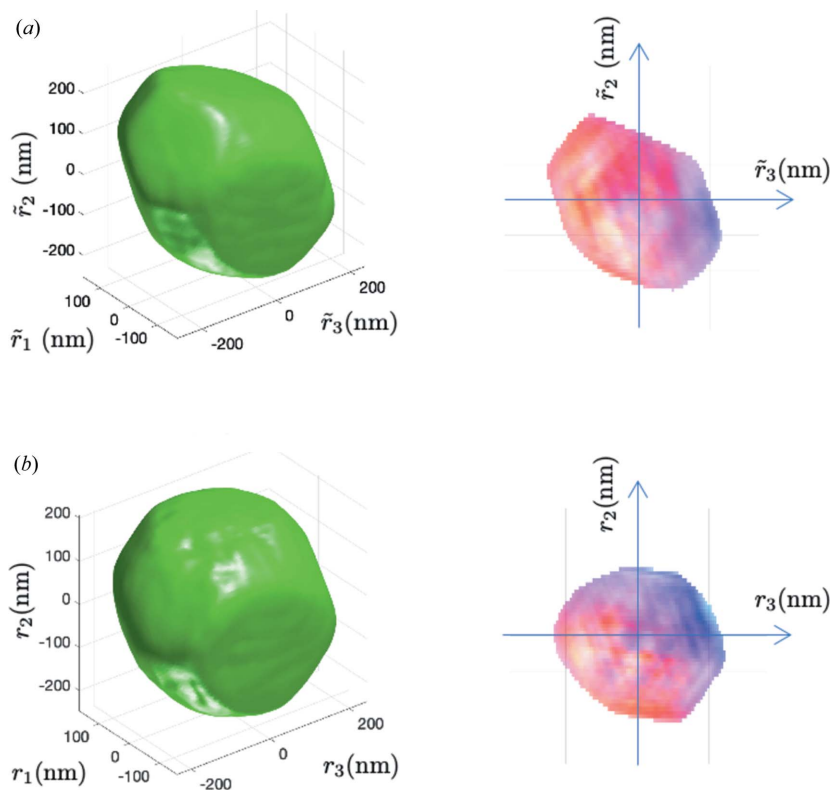


Figure 6 Reconstruction of a gold nanocrystal from experimental data obtained in a nonsymmetric case (*i.e.* not in a symmetric θ - 2θ geometry). (a) With a standard BCDI reconstruction, the sample estimate is built in a non-orthogonal frame $(\tilde{\mathbf{e}}_1, \tilde{\mathbf{e}}_2, \tilde{\mathbf{e}}_3)$. (b) In comparison, the orthogonal BCDI reconstruction strategy provides an ‘unsheared’ representation of the nanocrystal. Both reconstructions (a) and (b) were obtained with shrinkwrap and ER; the standard form of ER was used in (a), whereas the modified form used in (b) was derived from Appendices A and B. The experimental parameters that are associated with this experiment are given in Table 1.

and where $m_3 \in \mathbb{Z}$ and $(n_1, n_2) \in \mathbb{Z}^2$. The details of deriving the vector \mathbf{b} require a detailed knowledge of the sample goniometer motions and of the angular degrees of freedom of the detector. In particular, \mathbf{b} can be derived from equation (37) in Part I: it is the third column of the matrix $\mathbf{B}_{\text{det}}^T \mathbf{B}_{\text{recip}}$ scaled so that it is of unit norm.

For the sake of illustration, we show in Fig. 6 the reconstruction of a gold nanocrystal from experimental data obtained with the 34-ID-C coherent Bragg diffraction end station at the Advanced Photon Source. As indicated by the experimental parameters given in Table 1, this scan was performed in a nonsymmetric case since we have $\gamma \neq 0$ and $\delta \neq 0$ simultaneously (see Fig. 2 in Part I for a description of the degrees of freedom specific to this beamline). The reconstructions in Fig. 6 show how the geometrical distortions inherent with the non-orthogonal sampling geometry can be

Table 1

Experimental parameters of the gold nanocrystal BCDI scan, measured at Beamline 34-ID-C at the Advanced Photon Source.

Refer to Part I, Fig. 2, for the experimental geometry.

Parameter	Value	Description
E	9 keV	Beam energy
λ	1.378 Å	Wavelength
θ	0.1899°	Sample alignment
$\Delta\theta$	0.01°	Angular increment
D	0.635 m	Object–detector distance
γ	−14.05°	Detector alignment (elevation)
δ	30.1°	Detector alignment (azimuth)
p	55×10^{-6} m	Pixel size
(N_1, N_2, N_3)	(256, 256, 150)	Data array dimensions

avoided by the reconstruction strategy derived from Appendices A and B.

Required:

```
dp : stack of intensity patterns [array:  $N_2 \times N_1 \times N_3$ ]
psi : starting estimate [array:  $N_2 \times N_1 \times N_3$ ]
supp : support of the 3D exit field in the orthogonal frame [array:  $N_2 \times N_1 \times N_3$ ]
dq1, dq2, dq3 : Fourier-space sampling rates along  $k_1, k_2$  and  $k_3$  [scalars]
thetaB : Bragg angle [scalar]
```

Result:

```
psi : retrieved sample in the ORTHOGONAL representation [array:  $N_2 \times N_1 \times N_3$ ].
```

```
%% ER script
[N2,N1,N3] = size(dp);
dr1 = 1/(N1*dq1); dr2 = 1/(N2*dq2); dr3 = 1/(N3*dq3);
r1 = 0:dr1:(N1-1)*dr1; r2 = 0:dr2:(N2-1)*dr2; r3 = 0:dr3:(N3-1)*dr3;
q1 = 0:dq1:(N1-1)*dq1; q2 = 0:dq2:(N2-1)*dq2; q3 = 0:dq3:(N3-1)*dq3;
[R1,R2,R3] = meshgrid(r1,r2,r3); [Q1,Q2,Q3] = meshgrid(q1,q2,q3);
%% Pre-computation of the 3D modulation array
phase_ramp = exp(i*2*pi*R2.*Q3*tan(thetaB));
param = [dr1, dr2, dr3, thetaB];
%% The ER main loop
iter_num = 10; % Total number of ER update
alpha = 1; % Updating stepsize for ER
for iter = 1 : iter_num
    % Forward calculation: expected 3D far-field
    PSI_non_ortho = Real2NOF (psi, phase_ramp, param);
    % Modulus constraint in Fourier space:
    PSI_non_ortho = sqrt(dp).*exp(1i*angle(PSI_non_ortho));
    % backward calculation: corrected exit-field
    psi_new = NOF2Real (PSI_non_ortho, phase_ramp, param);
    % Real-space support constraint
    psi = psi - alpha*supp.*(psi - psi_new);
end
%% Forward and backward transformation functions...
function PSI_non_ortho = Real2NOF(psi, phase_ramp, param)
dr1 = param(1); dr2 = param(2); dr3 = param(3); thetaB = param(4);
scaling = cos(thetaB)*dr1*dr2*dr3;
XI_rx = fftshift(fft(psi, [], 3), 3).*phase_ramp*scaling
PSI_non_ortho = fftshift(fft(fftshift(fft(XI_ortho_rx, [], 1), 1), [], 2), 2);
end
function psi = NOF2Real (PSI_non_ortho, phase_ramp, param)
dr1 = param(1); dr2 = param(2); dr3 = param(3); thetaB = param(4);
scaling = cos(thetaB)*dr1*dr2*dr3;
zeta_r3 = fftshift(ifft(ifft(PSI_non_ortho, [], 1), [], 2), 3).*conj(phase_ramp);
psi = ifft(ifftshift(zeta_rx, 3), [], 3)/scaling;
end
```

Figure 7

MATLAB script for the error-reduction strategy, retrieving the orthogonal representation of the exit field ψ from the intensity of the non-orthogonal representation of the 3D diffracted field Ψ .

Required:

dp : stack of intensity patterns [array: $N_2 \times N_1 \times N_3$]
psi : starting estimate [array: $N_2 \times N_1 \times N_3$]
supp : support of the 3D exit field in the orthogonal frame [array: $N_2 \times N_1 \times N_3$]
dq1, dq2, dq3 : sampling rates along k_1 , k_2 and k_3 [scalars]
thetaB : Bragg angle [scalar]

Result:

psi : retrieved sample in the ORTHOGONAL representation [array: $N_2 \times N_1 \times N_3$].

```

%% ER script (project/back-projection version)
[N2,N1,N3] = size(dp);
dr1 = 1/(N1*dq1); dr2 = 1/(N2*dq2); dr3 = 1/(N3*dq3);
r1 = 0:dr1:(N1-1)*dr1; r2 = 0:dr2:(N2-1)*dr2; r3 = 0:dr3:(N3-1)*dr3;
q1 = 0:dq1:(N1-1)*dq1; q2 = 0:dq2:(N2-1)*dq2; q3 = 0:dq3:(N3-1)*dq3;
[R1,R2,R3] = meshgrid(r1,r2,r3);
[Q1,Q2,Q3] = meshgrid(q1,q2,q3);
scaling = cos(thetaB)*dr1*dr2;

%% The ER main loop
iter_num = 10; % Total number of ER update
alpha = 1; % Updating stepsize for ER
for iter = 1 : iter_num
    psi_ortho_new = 0;
    % Loop over the RC angles...
    for n_q3 = 1:N3
        sqrtI = squeeze(dp_sqr(:,:,n_q3));
        % Computation of the current slice in the 3D expected far-field...
        phase_ramp = exp(1i*2*pi*q3(n_q3)*(R3 - tan(theta_B)*R2));
        psi_mod_integ = squeeze(sum(psi_ortho.*conj(phase_ramp),3))*dr3;
        PSI_non_ortho = fftshift(fft2(fftshift(psi_mod_integ)))*scaling;
        % Contribution to the 3D corrected far-field
        PSI_non_ortho = sqrtI.*exp(1i*angle(PSI_non_ortho));
        psi_mod_integ = ifftshift(ifft2(ifftshift(PSI_non_ortho)))/scaling;
        psi_ortho_new = psi_ortho_new + ...
            repmat(psi_mod_integ, [1,1,length(q3)].*phase_ramp/(N3*dr3);
    end
    % Apply the support constraint...
    psi_ortho = psi_ortho - alpha*supp.*(psi_ortho - psi_ortho_new);
end

```

Figure 8

The same as in Fig. 7 but with projection and back-projection operators. We consider in this script that the RC is evenly sampled, with a sampling rate of about q_3 which meets the requirement $\delta_{q_3} = \delta_{\bar{q}_3} \cos \theta_B$ [see (22)].

APPENDIX B MATLAB codes

This appendix provides the MATLAB code of the modified ER phase-retrieval algorithms that reconstruct an image of the sample in the orthogonal real-space frame (\mathbf{e}_1 , \mathbf{e}_2 , \mathbf{e}_3). The code in Fig. 7 is derived from Section 3.3 and allows the 3D intensity data stack to be processed when the RC is evenly sampled. The projection/back-projection version of ER given in Fig. 8. This approach allows an arbitrary set of angles to be used for phase retrieval and employs the framework introduced in Section 4.3.

The aim of the codes presented in this appendix is to illustrate that the modified ER code is not very different from that currently in use for BCDI phase retrieval. The main difference is that the commands `fftn/ifftn` used to link the sample to the 3D field in the Fraunhofer regime are replaced by a different pair of functions. For example, these functions are `Real2NOF()` and `NOF2Real()` in Fig. 7. In the example codes, the number of mesh points N_1 and N_3 are the number of physical pixels extracted from the detector in q_1 and the number of angles in the RC, respectively. For the sake of

simplicity, we did not consider the extent of the Fourier domain in q_2 discussed in Section 3.3. As a result, N_2 is identical to the number of physical pixels extracted from the detector in q_2 . The origins of real and Fourier space are set to correspond to the central pixel of the respective numerical windows, which indicates that `fftshift/ifftshift` have to be used in combination with the Fourier transformations.

Finally, we note that other standard phase-retrieval algorithms such as HIO and shrinkwrap can be generated easily by adapting the ER codes provided. Source codes are available on request or can be downloaded directly from the repository set up by M. Allain & P. Li (<https://github.com/siddharth-maddali/BCDIGeometry-part2-reconstructioncode>).

Funding information

The development and simulations of the shear-aware Fourier transformation formalism for regularly sampled rocking curves based on the discrete Fourier transformation were supported by the European Research Council (European

Union's Horizon H2020 research and innovation program grant agreement No. 724881). The development of the back-projection-based Fourier transformation formalism for irregularly sampled rocking curves was supported by the US Department of Energy (DOE), Office of Science, Basic Energy Sciences, Materials Science and Engineering Division. This research uses the resources of the Advanced Photon Source, a DOE Office of Science User Facility operated for the DOE Office of Science by Argonne National Laboratory under contract No. DE-AC02-06CH11357.

References

- Berenguer, F., Godard, P., Allain, M., Belloir, J.-M., Talneau, A., Ravy, S. & Chamard, V. (2013). *Phys. Rev. B*, **88**, 144101.
- Calvo-Almazán, I., Allain, M., Maddali, S., Chamard, V. & Hruszkewycz, S. (2019). *Sci. Rep.* **9**, 6386.
- Cha, W., Ulvestad, A., Allain, M., Chamard, V., Harder, R., Leake, S., Maser, J., Fuoss, P. H. & Hruszkewycz, S. O. (2016). *Phys. Rev. Lett.* **117**, 225501.
- Chapman, H. & Nugent, K. (2010). *Nat. Photon.* **4**, 833.
- Clark, J., Huang, X., Harder, R. & Robinson, I. (2012). *Nat. Commun.* **3**, 993.
- Godard, P., Carbone, G., Allain, M., Mastropietro, F., Chen, G., Capello, L., Diaz, A., Metzger, T., Stangl, J. & Chamard, V. (2011). *Nat. Commun.* **2**, 568.
- Hill, M., Calvo-Almazan, I., Allain, M., Holt, M., Ulvestad, A., Treu, J., Koblmüller, G., Huang, C., Huang, X., Yan, H., Nazaretski, E., Chu, Y., Stephenson, G. B., Chamard, V., Lauhon, L. & Hruszkewycz, S. (2018). *Nano Lett.* **18**, 811–819.
- Hruszkewycz, S. O., Allain, M., Holt, M. V., Murray, C. E., Holt, J. R., Fuoss, P. H. & Chamard, V. (2017). *Nat. Mater.* **16**, 244–251.
- Hruszkewycz, S. O., Holt, M. V., Murray, C. E., Bruley, J., Holt, J., Tripathi, A., Shpyrko, O. G., McNulty, I., Highland, M. J. & Fuoss, P. H. (2012). *Nano Lett.* **12**, 5148–5154.
- Marchesini, S., He, H., Chapman, H. N., Hau-Riege, S. P., Noy, A., Howells, M. R., Weierstall, U. & Spence, J. C. H. (2003). *Phys. Rev. B*, **68**, 140101.
- Mastropietro, F., Godard, P., Burghammer, M., Chevallard, C., Daillant, J., Duboisset, J., Allain, M., Guenoun, P., Nouet, J. & Chamard, V. (2017). *Nat. Mater.* **16**, 946–952.
- Miao, J., Ishikawa, T., Robinson, I. K. & Murnane, M. M. (2015). *Science*, **348**, 530–535.
- Nishino, Y., Miao, J. & Ishikawa, T. (2003). *Phys. Rev. B*, **68**, 220101.
- Pfeifer, M. A., Williams, G. J., Vartanyants, I. A., Harder, R. & Robinson, I. K. (2006). *Nature*, **442**, 63–66.
- Robinson, I. K., Pfeiffer, F., Vartanyants, I. A., Sun, Y. & Xia, Y. (2003). *Opt. Express*, **11**, 2329–2334.
- Sayre, D. (1952). *Acta Cryst.* **5**, 843.
- Takagi, S. (1969). *J. Phys. Soc. Jpn.* **26**, 1239–1253.
- Ulvestad, A., Singer, A., Clark, J. N., Cho, H. M., Kim, J. W., Harder, R., Maser, J., Meng, Y. S. & Shpyrko, O. G. (2015). *Science*, **348**, 1344–1347.
- Vartanyants, I. & Robinson, I. (2001). *J. Phys. Condens. Matter*, **13**, 10593–10611.
- Williams, G. J., Pfeifer, M. A., Vartanyants, I. A. & Robinson, I. K. (2003). *Phys. Rev. Lett.* **90**, 175501.
- Yang, D., Phillips, N. W. & Hofmann, F. (2019). *J. Synchrotron Rad.* **26**, 2055–2063.